Materials Today Energy 52 (2025) 101936

Contents lists available at ScienceDirect

Materials Today Energy

journal homepage: www.journals.elsevier.com/materials-today-energy/

Enhanced thermoelectric properties of spin-assisted organic multilayered nanocomposite films

Sanghoon Jeong [a], You-yeong Byun [a], Junho Jang [b], Mario Culebras [c], Jung Sang Cho [d,*], Chungyeon Cho [a,e,**]

[a] Department of Carbon Convergence Engineering, College of Engineering, Wonkwang University, Iksan, 54538, Republic of Korea
[b] Insulation Materials Research Center, Electrical Materials Research Division, Korea Electrotechnology Research Institute (KERI), Changwon-si, 51543, Republic of Korea
[c] Institute of Materials Science (ICMUV) Catedrático José Beltrán, 2, Paterna, València, 46980, Spain
[d] Department of Engineering Chemistry, Chungbuk National University, Chungbuk, 361-763, Republic of Korea
[e] Department of Biomedical Materials Science, Jeonbuk Advanced Bio-convergence Academy, Wonkwang University, Iksan, Jeonbuk, 54538, Republic of Korea

ARTICLE INFO

Keywords:
Thermoelectric
Layer-by-layer
Organic multilayers
Spin coating
Graphene oxide
Polymer nanocomposites

ABSTRACT

This study presents a high-performance organic thermoelectric (TE) nanocomposite film fabricated via a spin-assisted layer-by-layer (LbL) assembly using poly(4-vinylpyridine-co-styrene) (PVPS), double-walled carbon nanotubes (DWNT), and graphene oxide (GO). Multilayers were constructed by alternately depositing positively charged PVPS and negatively charged DWNT-GO dispersions, followed by chemical reduction using L-ascorbic acid and subsequent thermal treatment. This dual-step reduction effectively restored the sp^2 carbon network and enhanced carrier mobility. The optimized 8-bilayer PVPS/DWNT-rGO film exhibited an electrical conductivity of 556 S/cm, a Seebeck coefficient of 105 μV/K, and a power factor of 612.5 μW/m·K^2 at room temperature. The synergistic interface design provided energy filtering and hierarchical charge transport, enabling simultaneous enhancement of conductivity and Seebeck coefficient. Structural analyses confirmed the formation of an interconnected, three-dimensional conjugated network, where DWNT bridge rGO platelets within the polymer matrix. This study is the first to report the fabrication of high-performance TE nanocomposites using a spin-assisted LbL assembly technique. These findings demonstrate that spin-assisted LbL assembly combined with green reduction strategies offers a scalable route to high-performance, flexible TE materials, potentially overcoming limitations of conventional inorganic systems and enabling next-generation waste-heat recovery and wearable energy-harvesting devices.

1. Introduction

The global energy crisis and environmental challenges have spurred intense interest in sustainable energy harvesting technologies. Among these, thermoelectric (TE) materials have emerged as a promising solution for converting waste heat into useful electrical energy. The efficiency of TE materials is typically described by the dimensionless figure of merit, ZT, given as: $ZT = \sigma S^2 T/\kappa$, where σ is the electrical conductivity, S is the Seebeck coefficient, T is the absolute temperature, and κ is the thermal conductivity. Achieving a high ZT value requires an optimal balance of these parameters, which poses a significant challenge due to their interdependence [1]. Recent advancements in nanostructured TE materials and hybrid composites have demonstrated potential to enhance ZT, enabling efficient energy recovery from industrial processes, automotive systems, and even human body heat [2,3].

Inorganic TE materials, such as bismuth telluride (Bi_2Te_3), lead telluride (PbTe), and tin selenide (SnSe), have demonstrated exceptional TE performance due to their high S and low κ [4]. However, these materials often suffer from limitations such as scarcity of raw materials, high cost, and poor mechanical flexibility, which restrict their scalability and application in wearable or flexible devices [5,6]. In contrast, organic TE materials, based on conductive polymers and carbon

* Corresponding author.
** Corresponding author. Department of Biomedical Materials Science, Jeonbuk Advanced Bio-convergence Academy, Wonkwang University, Iksan, Jeonbuk 54538, Republic of Korea.
E-mail addresses: jscho@chungbuk.ac.kr (J.S. Cho), cncho37@wku.ac.kr (C. Cho).

https://doi.org/10.1016/j.mtener.2025.101936
Received 22 April 2025; Received in revised form 29 May 2025; Accepted 6 June 2025
Available online 6 June 2025

nanomaterials such as graphene or carbon nanotubes, offer unique advantages [7,8]. These include lightweight properties, mechanical flexibility, low toxicity, and ease of large-scale processing. Moreover, the synergistic integration of conductive polymers with carbon nanomaterials enhances σ while maintaining low κ, making them highly attractive for next-generation TE applications [9,10].

Graphene oxide (GO), a chemically oxidized form of graphene, has attracted significant attention in TE studies due to its large surface area, high σ, and facile functionalization [11,12]. However, abundant oxygen-containing groups (hydroxyl, epoxy, carbonyl, carboxyl) in GO structures disrupt the sp^2 carbon network, substantially reducing conductivity compared to graphene [13]. Its relatively low intrinsic σ and the challenges associated with controlling its reduction level can limit TE properties when used alone. Improving conductivity of GO is thus critical for electronic applications. Conventional reduction methods use toxic reagents including hydrazine or NaOH, raising safety and environmental concerns [14,15]. In contrast, green reductants such as $_L$-ascorbic acid ($_L$-AA) or low-temperature thermal treatment offer safer, eco-friendly alternatives [16,17]. These methods effectively eliminate oxygen groups while preserving the carbon framework. Particularly, thermal reduction provides a simple and scalable approach to obtain conductive, few-layer graphene with enhanced electrical properties and reduced agglomeration.

The layer-by-layer (LbL) assembly technique is a versatile method for fabricating thin films with tailored properties [18,19]. While the traditional dipping method has been widely used for its simplicity and uniformity, spin coating has recently gained attention for its superior process efficiency, scalability, and material utilization [20,21]. Unlike dipping, which involves lengthy immersion and rinsing steps, spin coating allows for rapid layer deposition within seconds, reducing processing time and contamination risk. This technique also minimizes precursor solution consumption, aligning with sustainable manufacturing practices. Spin coating enables precise control of film thickness and uniformity by adjusting parameters such as spin speed, time, and solution concentration [22]. This level of control facilitates tuning of mechanical, optical, and thermal properties. Additionally, the centrifugal force promotes strong interlayer adhesion, improving mechanical integrity [23]. Given these advantages, spin coating-based LbL assembly has emerged as a promising alternative for applications requiring high throughput, uniformity, and cost-effectiveness. Its successful implementation across various polyelectrolytes and nanoparticles further highlights potential for scalable, precision-driven film fabrication.

In an effort to develop organic TE materials with a high power factor ($PF = \sigma S^2$), multilayered polymer nanocomposites composed of poly(4-vinylpyridine-co-styrene) (PVPS) and double-walled carbon nanotubes (DWNT), stabilized with graphene oxide (GO), were fabricated using a spin-assisted LbL assembly approach. Subsequently, these multilayer films underwent chemical reduction with $_L$-AA and further followed by thermal treatment. Among various types of carbon nanotubes, DWNT were selected in this study due to their unique structural features and favorable electrical properties. Compared to single-walled and multi-walled carbon nanotubes, DWNT offer an optimal balance between mechanical stability and electrical conductivity. Notably, the π–π interaction between the inner and outer walls of DWNT provides additional conduction pathways, leading to improved carrier mobility and enhanced TE performance in nanocomposite systems. Initially, an 8-bilayer PVPS/DWNT-GO thin film (~450 nm thick) exhibited relatively low σ (0.28 S/cm). However, chemical reduction with $_L$-AA significantly enhanced the σ to 368 S/cm, accompanied by an increased S of 95 μV/K, yielding an impressive PF of 331.8 μW/m·K^2. Furthermore, subsequent thermal treatment at 175 °C for 90 min resulted in additional improvements, achieving an σ of 556 S/cm and S of 105 μV/K. Consequently, a remarkably high PF of 612.5 μW/m·K^2 was obtained.

2. Materials and Methods

2.1. Materials

Double-walled carbon nanotubes (DWNT, XB type, diameter approximately 3 nm, length approximately 1 μm) were obtained from Continental Carbon Nanotechnologies, Inc. (Houston, TX, USA). Poly(4-vinylpyridine-co-styrene) (PVPS) and $_L$-ascorbic acid ($_L$-AA, Mw = 176.12 g/mol) were purchased from Sigma-Aldrich (St. Louis, MO, USA). 0.03 wt% DWMT were dispersed in 0.1 wt% graphene oxide (GO, CheapTubes, USA). A homogeneous dispersion of DWNTs with GO in water was achieved by initial bath sonication for 30 min, followed by tip sonication at 15 W for 40 min, and subsequently an additional bath sonication for 30 min. The resulting dispersion was centrifuged at 4000 rpm, and the supernatant was carefully collected. In order to study the performance of two steps post-treatments toward the deoxygenation of GO, as-assembled films were reacted at 80 °C for 40 min with a 0.2 wt% $_L$-AA solution, as shown in Fig. S1. In order to further reduce, these films were thermally treated by exposing them in an oven (175 °C for 90 min). All chemicals were used as received. Deionized (D.I) water (Milli-Q, Billerica, MA) with a specific resistance greater than 18 MΩ was used in all aqueous solutions.

2.2. Substrates

Polyethylene terephthalate (PET) film (trade name: ST 505; thickness: 179 μm), manufactured by DuPont Teijin and purchased from Tekra Corporation (New Berlin, WI, USA), was employed as the substrate for thermoelectric measurements and Transmission electron microscopy (TEM) images. Before deposition, PET substrates were thoroughly cleaned by sequential rinsing with methanol and D.I water, followed by surface activation via corona treatment (BD-20C corona treater, Electro-Technic Products Inc., Chicago, IL, USA) to enhance the adhesion properties of the initial deposited layer through surface oxidation. Single-side-polished silicon wafers (Si-wafers, thickness: 500 μm, orientation: (100)), supplied by University Wafer (South Boston, MA, USA), served as substrates for surface characterization analyses. Prior to use, Si-wafers were sequentially cleaned using acetone, methanol, and D.I water, and subsequently subjected to plasma treatment for 5 min using a plasma cleaner (Harrick Plasma, Ithaca, NY, USA).

2.3. Film deposition

PVPS/DWNT-GO multilayer thin films were fabricated using a spin-assisted LbL deposition technique, wherein positively charged PVPS and negatively charged DWNT-GO suspensions were alternately assembled onto various substrates, including Si-wafers, PET films, and quartz slides. Specifically, each substrate was initially mounted onto a spin coater (ACE-200, Dong-Ah Corp., South Korea) and rotated at a controlled speed of 3000 rpm. A precisely measured droplet (150 μL) of positively charged PVPS solution (0.25 wt%) was dispensed onto the spinning substrate and allowed to spread uniformly for 20 s, forming an evenly coated polyelectrolyte layer. Subsequently, an equivalent volume of the negatively charged DWNT-GO suspension was deposited onto the PVPS layer under identical spinning conditions to form a bilayer structure. This alternating deposition process was repeated until the desired number of PVPS/DWNT-GO bilayers was successfully assembled, thereby achieving multilayer thin films with controlled thickness and uniformity.

2.4. Characterization

The thickness of multilayer films deposited on Si-wafers was determined using a stylus profilometer (NanoMap-PS, AEP Technology, Santa Clara, CA, USA). To measure the film thickness accurately, multiple parallel scratches were carefully introduced into each sample, and the

average height difference between the film surface and the substrate was recorded. The final reported thickness represents an average calculated from at least 10 independent measurements per sample. The surface morphology and topographical characteristics of the multilayered films prepared on Si-wafers were examined using AFM (Nanostation Surface Imaging Systems, Herzogenrath, Germany) and SEM (Hitachi, Japan). TEM was carried out to investigate the internal microstructure of the deposited materials using a JEOL JEM-1010 microscope operating at an acceleration voltage of 100 kV. The chemical composition and structural properties of both pristine and reduced PVPS/DWNT-GO multilayers were characterized by XPS (Omicron NanoTechnology, Taunusstein, Germany) and Raman spectroscopy (DXR Raman microscope, Thermo Fisher Scientific, Milan, Italy). The mechanical property such as elastic modulus of the films was measured using an ultra-nanoindentation instrument (UNHT3, Anton Paar, Switzerland) equipped with a spheroconical indenter tip (tip radius: 2 μm, cone angle: 90°).

2.5. Thermoelectric measurements

A standard four-point probe (CMT-100S, Advanced Instrument Technology) was used to measure the sheet resistances (*Rs*) of the LbL samples deposited on the PET substrates. Electrical conductivity (σ) was calculated as $\sigma = (Rs \bullet t)^{-1}$, where t is the thickness of the multilayer thin films. Before conducting the measurements, all of the samples were cut to the required dimensions (30 mm in length and 10 mm in width). The Seebeck coefficient was obtained with a four-point probe setup designed to measure electrical voltage ($\Delta V = V_{cold} - V_{hot}$) and temperature difference ($\Delta T = T_{hot} - T_{cold}$). Carrier density and mobility were evaluated at room temperature using Hall effect measurements performed in the van der Pauw configuration (sample dimensions: 20 mm × 20 mm) with an Ecopia HMS-3000 measurement system (Ecopia Corp., South Korea). To improve measurement accuracy and reproducibility, each specimen was subjected to 20 repeated measurements at three different applied currents (50, 100, and 150 μA) under a stable magnetic field strength of 1 T. An X-ray photoelectron spectroscope (Sigma Probe, Thermo VG Scientific) was used to acquire UPS data from the LbL thin films deposited on the Au-coated Si-wafers.

3. Results and discussion

3.1. Multilayer formation

Fig. 1(a) illustrates the LbL deposition process for constructing PVPS/DWNT-GO BL assemblies via the spin-coating technique. This method enables the controlled growth of multilayered thin films by sequentially adsorbing oppositely charged species onto a substrate. The corresponding chemical structures of the polymeric and carbon-based nanomaterials involved in this assembly are depicted in Fig. 1(b). Detailed experimental conditions, including the solution concentrations, spin-coating parameters, and deposition environment, are described in the Materials and Methods section. The LbL deposition of PVPS/DWNT-GO bilayers is based on the alternating adsorption of positively charged PVPS and negatively charged DWNT-GO complexes. The integration of DWNTs within the GO solution enhances the colloidal stability of the dispersion, facilitating a uniform film formation during each deposition cycle [24–26]. The electrostatic interactions between cationic PVPS and anionic DWNT-GO are the primary driving force governing the sequential adsorption, ensuring reproducible layer growth with controlled thickness and homogeneity. The cationic behavior of PVPS in aqueous solution originates from the partial protonation of its pyridine groups, forming pyridinium ions that impart a net positive charge. Conversely, the DWNT-GO dispersion exhibits anionic characteristics due to the deprotonation of carboxylic acid groups on the GO sheets, which adsorb onto DWNT surfaces and stabilize them in water. This charge complementarity enables electrostatic assembly between PVPS and DWNT-GO. A photo-image of DWNT in GO solution highlights the stability of these colloidal dispersions after sonication and centrifugation, indicating that the presence of GO prevents significant aggregation of the DWNT, a phenomenon that has been reported in previous studies utilizing carbon nanotube-based hybrid systems for LbL assembly (Fig. S2) [27,28]. Both AFM and SEM images of drop-cast dilute solutions on Si-wafers further revealed the homogeneous distribution of carbon nanotubes in GO, with minimal aggregation. This suggests that the incorporation of GO as a stabilizing agent effectively mitigates the intrinsic van der Waals forces between nanotubes, facilitating their integration into the multilayered architecture [29].

The film growth of PVPS/GO and PVPS/DWNT-GO BL assemblies deposited on Si-wafers was systematically analyzed using profilometry, focusing on the growth behavior as a function of the number of cycles, as depicted in Fig. 2. Both multilayered systems exhibited a linear increase in thickness, with growth increments of approximately 38 nm per BL for PVPS/GO and 56 nm per BL for PVPS/DWNT-GO. This linearity indicates the consistent incorporation of each component during each deposition cycle of the LbL assembly process. The observed higher growth rate in PVPS/DWNT-GO films compared to PVPS/GO is likely attributable to the three-dimensional architecture of the carbon

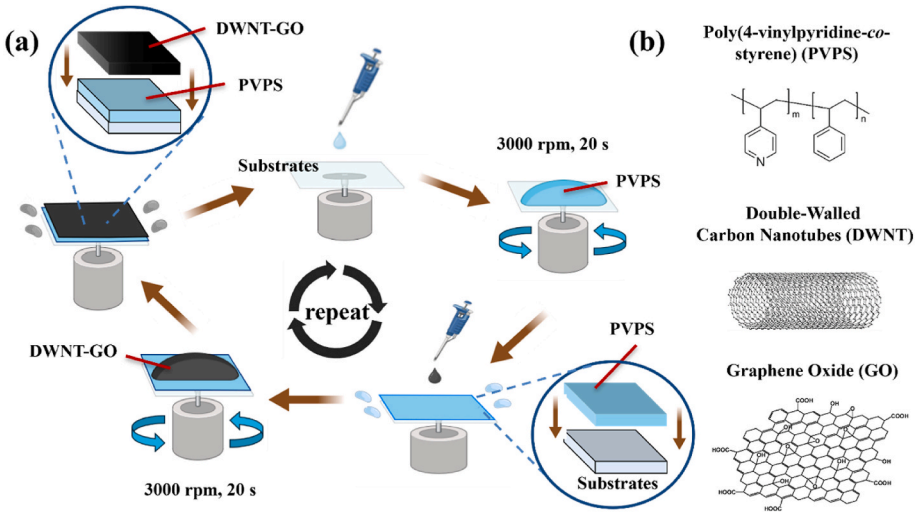

Fig. 1. (a) Schematic illustration of the layer-by-layer assembly for thermoelectric nanocomposites via spin coating process and (b) chemical structures of PVPS, DWNT, and GO used in this study.

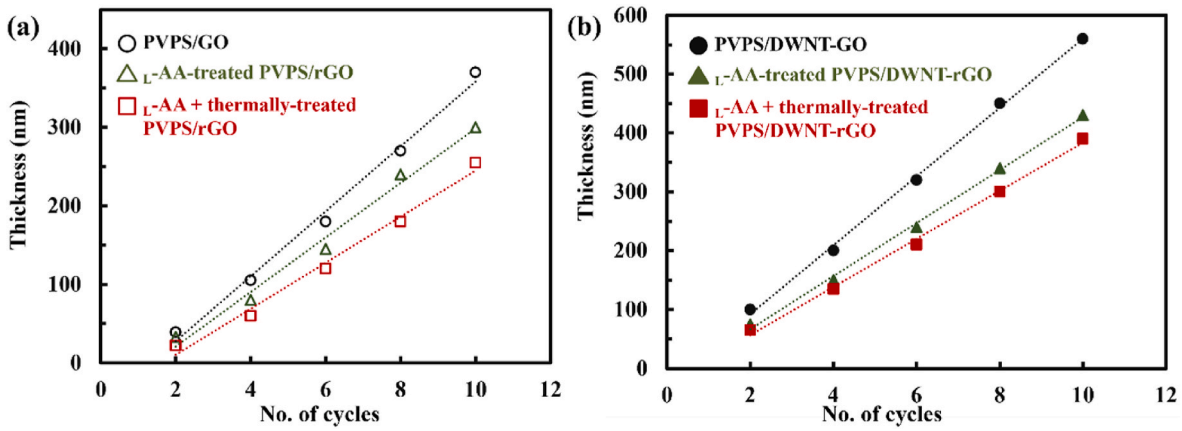

Fig. 2. Profilometric thickness analysis of spin-coated multilayers deposited on Si-wafers before and after post treatment (i.e., $_{L}$-AA reduction and low temperature treatment) of (a) PVPS/GO and (b) PVPS/DWNT-GO bilayer systems as a function of cycles. Post-treated PVPS/GO and PVPS/DWNT-GO systems are denoted as PVPS/rGO and PVPS/DWNT-rGO, respectively.

nanotubes, which can enhance layer thickness due to their structural characteristics. Similar linear growth behaviors have been reported in other studies involving multilayer thin films composed of carbon-based nanofillers, including carbon nanotubes, graphene, and graphene oxide [30–32]. Post-assembly treatments, such as chemical reduction and thermal treatment, significantly influence the thickness and properties of these multilayered films. Chemical reduction, using $_{L}$-ascorbic acid ($_{L}$-AA), caused shrinkage in film thickness, approximately 24.5 % for PVPS/GO films and 25.3 % for PVPS/DWNT-GO films. This reduction is attributed to the removal of oxygen-containing functional groups, leading to a more compact film structure. Additionally, thermal treatment induced a slight decrease (around 10 %) in film thickness, likely due to further deoxygenation of GO, resulting in densification of the film. These observations are consistent with findings from studies on LbL-assembled GO films, where thermal reduction led to decreased interlayer spacing [33]. Throughout this study, PVPS/GO and PVPS/DWNT-GO multilayer thin films are referred to as PVPS/rGO and PVPS/DWNT-rGO, respectively, following reduction treatments.

3.2. Thin film structures

The microstructure of the PVPS/DWNT-GO multilayers was extensively characterized using AFM, SEM, and TEM, as shown in Fig. 3. AFM images of the top surface of the two BL films revealed a uniform deposition of single GO platelets, with carbon nanotubes clearly distributed across their surfaces (Fig. 3(a)). Upon further deposition, the nanotubes formed increasingly dense, entangled networks (Fig. S3(a), Supporting Information), indicating nanotube aggregation and interconnection with additional layers. SEM analysis confirmed that individual nanotubes and bundles are well-distributed, creating a continuous conductive network across the film surface (Fig. 3(b)). This interconnected nanotube network effectively bridges GO platelets, facilitating electron conduction pathways throughout the multilayers. Even after four deposition cycles, an extensively interconnected nanotube network with high surface coverage was observed (Fig. S3(b)). The GO facilitates effective exfoliation and uniform dispersion of DWNT within the multilayer structure, promoting the formation of a three-dimensional conductive network characterized by nanotube entanglements resembling polymeric structures. The rope-like morphology observed for DWNT suggests that PVPS molecules wrapped around the nanotube surfaces, rather than forming distinctly separated alternating layers with the carbon nanotubes. After subsequent reduction treatments, the surface morphology of PVPS/DWNT-rGO multilayer films remained largely consistent with the original structure (as shown in Fig. S4, Supporting Information).

Detailed TEM characterization provided further insights into the internal architecture of PVPS/DWNT-GO assemblies. As depicted in Fig. 3(c), individual GO platelets (average diameter: 1~1.2 μm) coexist with a clearly observable network of DWNT underneath. The distinct contrast between GO platelets and DWNT emphasizes the uniform and dense distribution of nanotubes interconnecting the GO sheets (Fig. S5). The DWNT appeared randomly entangled, forming a three-dimensional (3D) network structure indicative of effective dispersion facilitated by GO-assisted exfoliation. A magnified view (inset in Fig. 3(c)) reveals that nanotube diameters of approximately 3 nm increased from their original ~2 nm size, suggesting polymers wrapping around the nanotubes. These interactions and network structures significantly contribute to enhanced electrical conduction, directly benefiting TE properties.

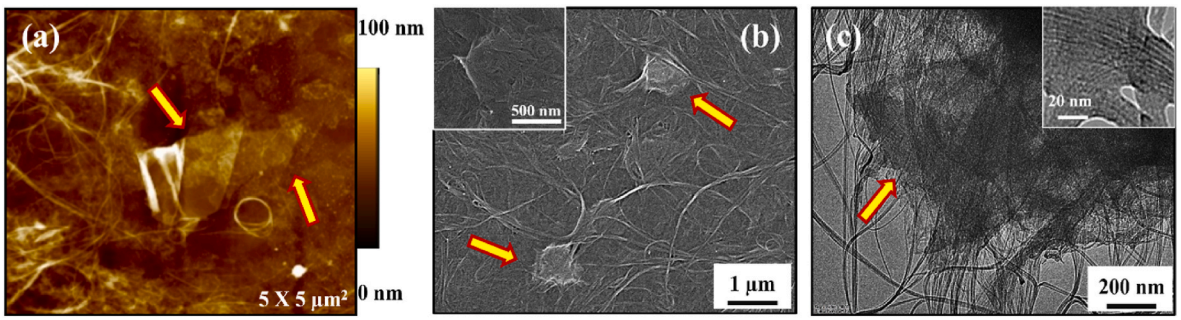

Fig. 3. (a) AFM, (b) SEM, and (c) TEM images of 2 BL spin-coated PVPS/DWNT-GO surface structures deposited on Si-wafers. Yellow arrows indicate exfoliated GO sheets on the surface in each surface image. Insets in (b) and (c) exhibit higher-resolution SEM and TEM images of GO and DWNT in the LbL thin films, respectively.

3.3. Thermoelectric properties

Electrical characterization was conducted by measuring the sheet resistance of PVPS/DWNT-GO multilayers assembled on PET substrates using the four-point probe method. The properties of PVPS/GO and PVPS/rGO systems are not plotted due to their low performance (i.e., sheet resistance >1 MΩ/sq). Although both GO and DWNT are frequently referred to as electrically conductive components, it is important to distinguish their individual roles in this study. GO exhibits poor electrical conductivity (σ) due to its high oxygen content, and thus PVPS/GO films showed negligible TE response. Meanwhile, DWNT, intrinsically conductive, lack sufficient surface charge to be directly assembled using the LbL method. In our approach, electrostatic assembly was only achieved via co-stabilization with negatively charged GO, enabling uniform dispersion and deposition. Therefore, PVPS/DWNT films could not be fabricated or evaluated separately, and the hybrid DWNT-GO system was essential to achieve stable LbL assembly and optimized TE performance. Fig. 4(a) illustrates the sheet resistance decrease from approximately 300 kΩ/sq at 4 BL to 65 kΩ/sq at 10 BL. Subsequent chemical reduction using $_L$-ascorbic acid ($_L$-AA) dramatically lowered sheet resistance to about 70 Ω/sq at 10 BL. Thermal treatments on chemically reduced PVPS/DWNT-rGO thin films further decreased resistance to achieve 48 Ω/sq at 10 BL. The observed gradual decrease in electrical resistance with increasing number of deposited bilayers confirms the progressive enhancement in electrical conductivity within these multilayer thin film assemblies. Corresponding σ, calculated from the reciprocal product of film thickness (Fig. 2(b)) and sheet resistance, increased with deposition cycles, reaching 0.27 S/cm at 10 BL prior to reduction. The $_L$-AA reduction to the PVPS/DWNT-GO system significantly improved the TE performances, achieving 368 S/cm at 8 BL. The observed increase in σ with the deposition of additional layers indicates enhanced formation and densification of conductive pathways, arising from the transition of the DWNT-GO network from a two-dimensional structure toward a highly interconnected 3D architecture. Beyond 8 BL, the rate of conductivity improvement diminished, reaching 335 S/cm at 10 BL, indicating the multilayer assembly surpassed its percolation threshold. The observed plateau in electrical conductivity beyond 8 BL suggests that the multilayer structure approaches a percolation threshold, where a continuous and interconnected conductive network is effectively established. While the exact critical volume fraction was not quantified in this study, the saturation trend in conductivity and the morphological uniformity observed in AFM analyses support this interpretation (Fig. S7). Above this point, additional deposition contributes more to film thickness than to enhancing the conductive network [34,35]. A more rigorous evaluation of the percolation behavior, such as effective medium modeling or filler volume analysis, will be addressed in future studies. Thermal treatment at 175 °C for 90 min further enhanced conductivity, achieving up to 556 S/cm at 8 BL. It is noteworthy that the reduction conditions employed were sufficiently gentle to preserve film integrity and material stability on PET substrates (175 μm thickness), as evidenced by the absence of material loss or structural degradation after the thermal treatment (Fig. S4).

TE performance was assessed by measuring the Seebeck coefficient (S) as a function of layer number (Fig. 5(a)). Positive S values confirmed p-type carrier transport. Initially, S gradually increased with additional layers, achieving 80 μV/K at 8 BL for untreated films. PVPS/DWNT-GO assemblies showed a gradual increase in S with adding layers, attaining 80 μV/K at 8 BL. An increase in S was observed following $_L$-AA reduction, achieving 95 μV/K. Additional thermal treatment on this PVPS/DWNT-rGO system increased S to attain 105 μV/K at 8 BL. Based on the σ and S, the power factor ($PF = S^2 \bullet \sigma$) of the spin-coated LbL nanocomposites was calculated at room temperature as the function of BL deposited. The PF of untreated PVPS/DWNT-GO system is plotted alone in the Supporting Information (Fig. S8) due to its relatively low value making it difficult to see in Fig. 5(b). The multilayer thin films exhibited an increase in PF analogous to σ with thickness. An 8 BL unreduced LbL assembly had a very low PF at room temperature (≈0.18 μW/m•K^2) while $_L$-AA treated multilayers were three orders of magnitude larger (≈331.8 μW/m•K^2). PVPS/DWNT-rGO films (~390 nm thick) after low temperature heat treatment achieved a PF as high as 612.5 μW/m•K^2 at 8 BL. Although the thermal conductivity of the multilayer films was not directly measured due to the submicron film thickness and associated experimental challenges, it is expected that the thermal conductivity would fall between 0.35 and 20 W/m•K based on other reports (Table S1). Given the highly nanostructured architecture of our LbL films, which introduces numerous interfaces to scatter heat-carrying phonons, it is reasonable to expect low thermal conductivity within this range. The estimated ZT value for the present films could be anywhere from 0.009 to 0.525 at room temperature.

To evaluate the benefits of the spin-assisted LbL strategy, a direct comparison was conducted with conventional drop-cast films of the same thickness (300 nm) after identical reduction treatments. As summarized in Table S2, the drop-coated films exhibited significantly lower TE performances, compared to the spin-coated multilayers. These results clearly demonstrate that the LbL process enables more effective nanostructure control, improved interfacial organization, and enhanced charge transport. The precise stacking of polymer and nanocarbon layers

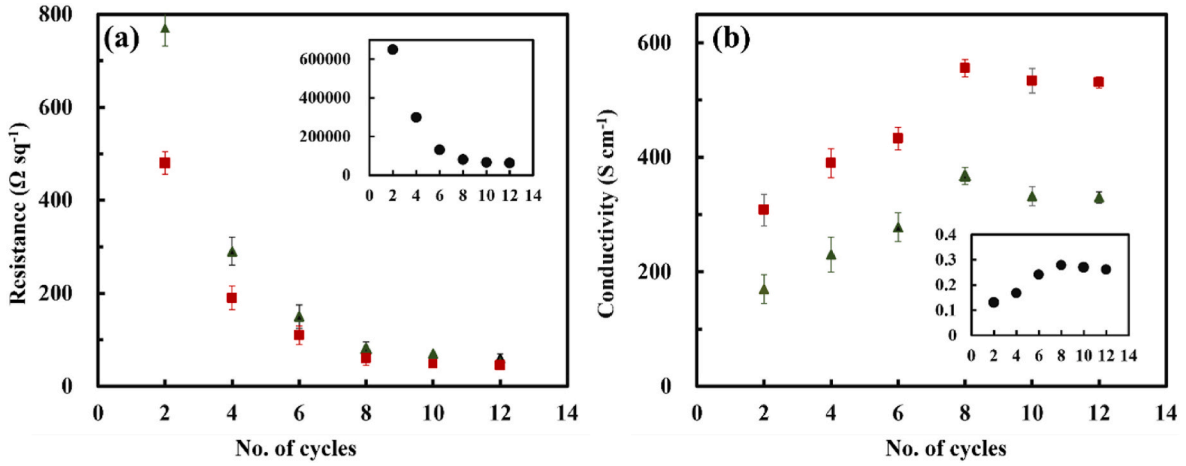

Fig. 4. (a) Sheet resistance and (b) electrical conductivity of PVPS/DWNT-rGO LbL thin films deposited on PET substrates as a function of the number of deposition cycles, after $_L$-AA reduction alone (triangle), and subsequent thermal reduction of chemically treated films (square). Insets in (a) and (b) indicate sheet resistance and electrical conductivity of PVPS/DWNT-GO multilayers. The electrical properties of unreduced systems alone are shown in Supporting Information Figure S6.

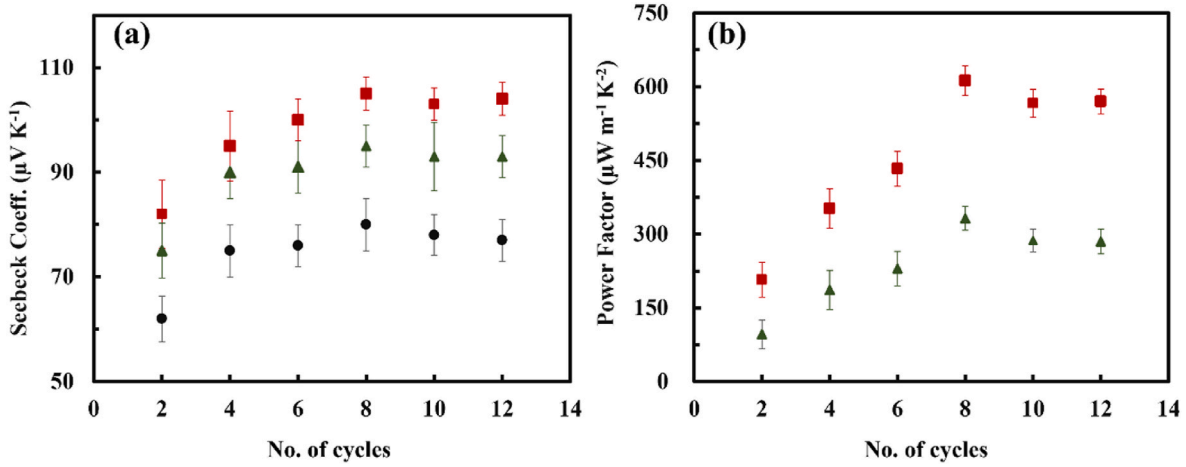

Fig. 5. (a) Seebeck coefficient and (b) power factor of spin-coated PVPS/DWNT-GO (circle) and PVPS/DWNT-rGO LbL thin films deposited on PET substrates as a function of the number of deposition cycles, after $_{L}$-AA reduction alone (triangle), and subsequent thermal reduction of chemically treated films (square). Power factors of PVPS/DWNT-GO alone are shown in Supporting Information Figure S8.

in the LbL architecture allows for optimized energy-filtering and efficient carrier mobility, leading to superior TE performance. Interestingly, the sequence of reduction treatments significantly influenced the resulting TE performances. When the LbL-assembled films were first chemically reduced using $_{L}$-AA and subsequently subjected to thermal treatment, a marked enhancement in the TE properties was observed. Conversely, multilayered thin films that was initially subjected to thermal annealing, followed by chemical reduction, exhibited negligible improvements in TE behaviors (Figs. S9 and S10). This suggests that thermal treatment was sufficient to convert most of the GO sheets to rGO by significantly removing oxygen functionalities. Consequently, the subsequent chemical reduction with $_{L}$-AA could not further reduce the already extensively reduced graphene structure, leading to minimal additional improvement. Thus, our findings clearly demonstrate the critical influence of the reduction treatment sequence on the TE performance of GO-based multilayer thin films, providing valuable insights into optimizing their TE efficiency via controlled reduction methods.

It is notable that the LbL-assembled multilayer thin films demonstrated a simultaneous improvement in both σ and S with increasing bilayer numbers. Such concurrent enhancement of thermoelectric

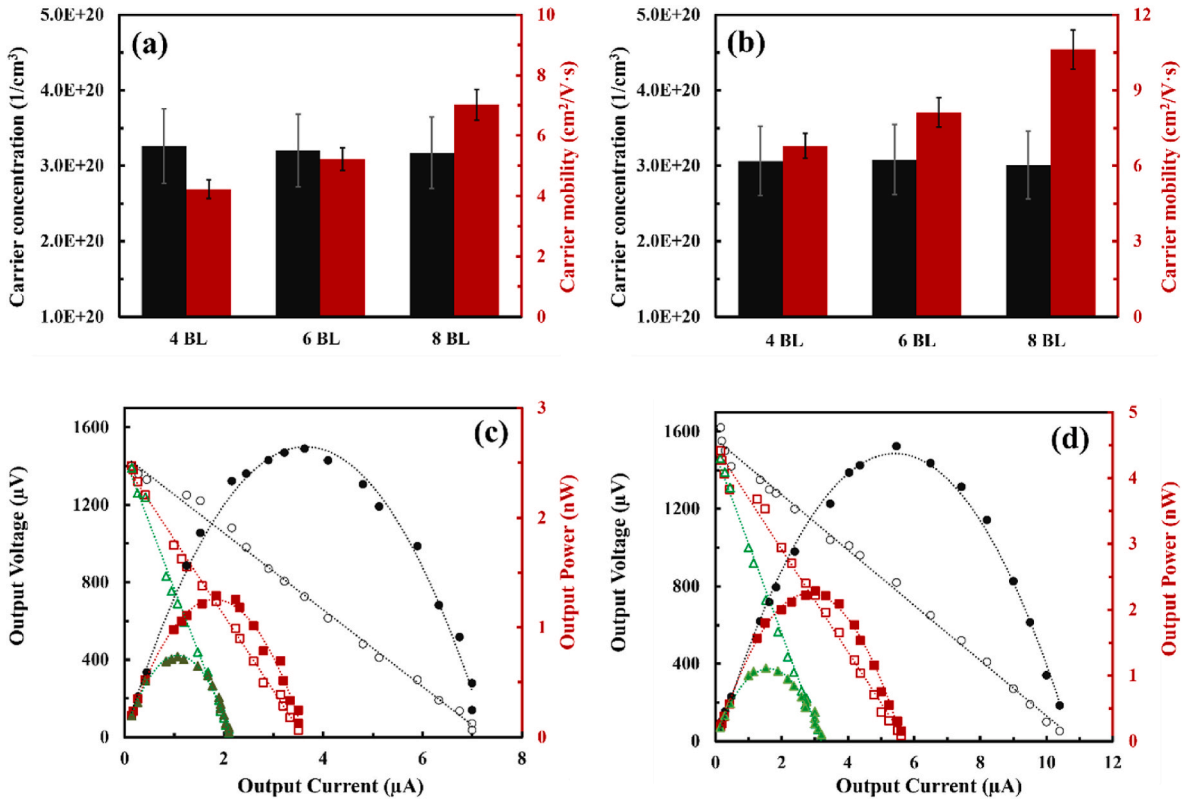

Fig. 6. Carrier concentration and carrier mobility of the spin-coated PVPS/DWNT-rGO LbL thin films after (a) $_{L}$-AA reduction alone, and (b) subsequent thermal reduction of chemically treated films. Output voltage (open symbols) and output power (closed symbols) of the spin-coated PVPS/DWNT-rGO multilayers films after (c) $_{L}$-AA reduction alone, and (d) subsequent thermal reduction of chemically treated films as a function of bilayers deposited at a temperature difference of 15.5 K. Circles, squares, and triangles indicate 4, 6, and 8 BL spin-coated LbL assemblies.

parameters is uncommon in traditional inorganic thermoelectric materials, where σ and S typically exhibit a strong inverse relationship [1,36,37]. In order to clarify the decoupled TE behaviors, the carrier concentration (n) and carrier mobility (μ) of the films were systematically characterized through Hall effect measurements conducted in the van der Pauw configuration, both before and after reduction treatments (Fig. 6(a), (b), and Fig. S11). The reported values for n and μ values represent the average of measurements taken from three independently prepared samples. Based on the relation of ($\sigma = ne\mu$, where e is the elementary charge), both untreated and reduced multilayers exhibited a slight decrease in n, while the μ increased with increasing layers from 4 to 8 BL. The n of $_L$-AA-treated PVPS/DWNT-rGO thin films exceeded that of PVPS/DWNT-GO films by less than a factor of three; however, the μ in these chemically reduced films was enhanced by two orders of magnitude. This large increase in mobility contributes to the high TE performance in the PVPS/DWNT-rGO films after $_L$-AA treatment. After subsequently subjected to thermal treatment of PVPS/DWNT-rGO multilayers, the μ was further increased, while n decreased slightly. The μ of chemically-reduced 8 BL PVPS/DWNT-rGO films increased by a factor of 1.66 relative to 4 BL, while the n decreased modestly from 3.26×10^{20} cm^{-3} at 4 BL to 3.17×10^{20} cm^{-3} at 8 BL. Subsequent thermal reduction of the $_L$-AA-treated LbL assemblies revealed that the μ of the 8 BL thin films was calculated to be 10.62 cm^2/V·s, representing an increase of more than 50 % compared to the mobility of 6.79 cm^2/V·s measured for the 4 BL multilayers. The observed concurrent increase in σ and S was primarily attributed to significantly enhanced carrier mobility facilitated by the highly ordered 3D conductive network, ultimately leading to notable power factor improvements [38,39].

In evaluating TE performance, maximizing both the output voltage and output power is critical, as these factors directly influence the efficiency and practical applicability of TE generators. The power output measurement from TE materials is fundamentally governed by the relationship $P = I \bullet V$, where P is the output power, I is the output current, and V is the output voltage. The TE output power of multilayer films (2 × 4 cm^2) was evaluated at room temperature. Fig. 6(c) and (d) show the output voltage and power as a function of output current, of the PVPS/DWNT-rGO thin films. Maximum output power (P_{max}) is attained when the external load (R_L) matched the internal resistance (R_i); $P_{max} = V_{oc}^2/4R_i$ (V_{oc} ~ open-circuit voltage). Both systems exhibited that TE power was proportional to the number of layers deposited. The combined chemical and thermal reduction treatments on GO-based LbL assemblies enhanced the σ, as evidenced by higher output voltage and power output values. As for the TE characteristics following an additional thermal reduction step after chemical treatment, maximum power of 8 BL PVPS/DWNT-rGO multilayers was 4.57 nW at $\Delta T = 15.5$ K from the current-power curves. This value represents a 1.69-fold enhancement compared to systems subjected solely to chemical reduction. It is clear that dual-step reduction ($_L$-AA treatments followed by low temperature reduction) leads to superior TE performance, attributed primarily to the efficient restoration of the graphene basal plane conjugation and improved carrier transport within the rGO nanosheets. Although the obtained power output remains insufficient for direct practical device implementation, the energy harvesting efficiency of modules utilizing the developed composites could be further improved through systematic optimization of device architecture and processing conditions.

3.4. Highly tunable thermoelectric behavior

The highly improved TE performance of spin-assisted PVPS/DWNT-GO nanocomposites can be attributed to a synergistic combination of two factors: (1) an effective conversion of GO to rGO via post-treatments and (2) the three-dimensionally conjugated carbon network, consisting of carbon nanotubes and rGO. Although GO platelets strongly interact with PVPS and DWNT, contributing to the uniform dispersion and stable assembly of DWNT within multilayer films, the abundant oxygen-containing functional groups (e.g., hydroxyl, carboxyl, and epoxy groups) present on GO surfaces and edges induce significant electron scattering and impede charge transport [40]. Consequently, PVPS/DWNT-GO multilayers exhibited relatively low σ. However, through chemical or thermal reduction treatments, partial restoration of the sp^2 carbon network transforms GO into rGO, substantially enhancing σ, as clearly demonstrated in Fig. 4(a) and (b). XPS analysis confirmed the effective removal of oxygen functionalities and restoration of conjugated carbon structures in the rGO sheets, as shown in Fig. 7(a). It is clearly demonstrated that chemical and thermal reduction processes effectively converted GO into rGO. Prior to reduction, the PVPS/DWNT-GO film exhibited a pronounced C1s peak at 286.1 eV, characteristic of significant oxygen-containing functional groups, primarily indicative of numerous C-O bonds [41]. After $_L$-AA treatment, a notable decrease in the intensity of the C1s peak at 286.1 eV (relative to the primary graphitic C-C peak at 284.2 eV) was observed, indicating the partial removal of these oxygen-containing groups and the restoration of the conjugated hexagonal carbon network [42]. Importantly, when the $_L$-AA-treated films were subsequently subjected to thermal reduction, the intensity of the C1s peak at 286.1 eV further diminished, indicating a more extensive removal of oxygen functional groups and enhanced recovery of graphitic domains.

In an effort to further investigate the structural changes and the recovery of conjugated sp^2 carbon networks in PVPS/DWNT-GO multilayer films during reduction, Raman spectroscopy was performed (Fig. 7(b)). The spectra displayed two prominent characteristic peaks; the D band (~1342 cm^{-1}), attributed to the sp^3 vibration of carbon atoms associated with structural defects and disorder in the graphene sheets due to extensive oxidation, and the G band (~1589 cm^{-1}), linked to the in-plane stretching vibrations of pairs of sp^2 carbon atoms reflecting ordered graphene domains [43,44]. Prior to reduction, the PVPS/DWNT-GO films exhibited a relatively high intensity ratio (I_D/I_G) of 0.36, implying considerable disruption and oxidation-induced disorder within graphene layers [45]. Upon chemical reduction using $_L$-AA, the I_D/I_G ratio notably decreased to 0.21, indicating successful partial restoration of sp^2 domains and the reduction of structural defects as oxygen functionalities were removed. Subsequent thermal reduction treatment after $_L$-AA reduction further decreased the I_D/I_G ratio to 0.11, indicating an enhanced recovery of graphitic order and further suppression of structural disorders. These Raman spectroscopy results strongly support that the combination of chemical reduction ($_L$-AA) followed by thermal treatment is highly effective in restoring the conjugated graphene structure, significantly reducing defects and disorder in PVPS/DWNT-rGO thin films. After thermal reduction, a red-shift in the G band was observed in the Raman spectra, which is associated with the structural recovery of the conjugated sp^2 domains. This shift can be attributed to (i) the removal of oxygen functional groups and restoration of π-conjugation, (ii) the relaxation of oxidative strain and decrease in defect density, and (iii) strong interfacial interactions between rGO, DWNTs, and the PVPS matrix. These phenomena collectively indicate improved graphitic order and are consistent with the enhanced electrical conductivity of the multilayer films.

The electronic structures of PVPS/DWNT-GO multilayer thin films were systematically investigated using UPS. According to Mott's formalism, the S is defined as $S(E,T) = \frac{\pi^2}{3}\frac{k^2T}{q}\left(\frac{\partial \ln(\sigma(E))}{\partial E}\right)_{E=E_f}$, indicating a direct relationship between the slope of the density of states (DOS) at the Fermi level (E_f) and the magnitude of S [46]. The UPS spectra revealed distinct differences between untreated and reduced films, clearly demonstrating that the reduction processes significantly modified the electronic structure (Fig. 8(a)). After chemical reduction with $_L$-AA, the slope of the UPS spectra became noticeably steeper compared to the untreated PVPS/DWNT-GO films, implying enhanced DOS variations around the Fermi level and thus suggesting an increase in S. The work function values obtained from UPS measurements showed shifts upon reduction treatments, which are indicative of altered E_f positions

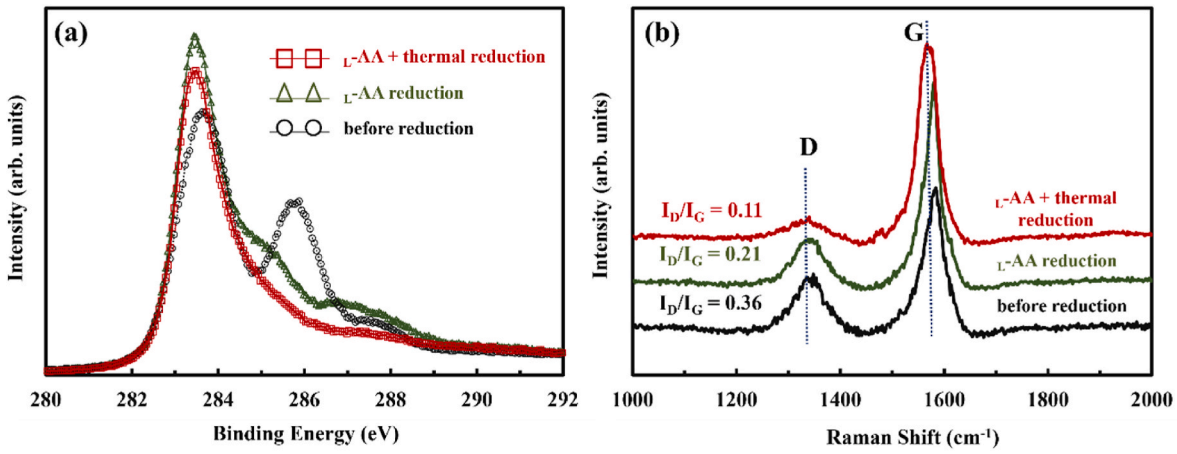

Fig. 7. (a) XPS and (b) Raman spectra of 8 BL spin-coated PVPS/DWNT-GO and PVPS/DWNT-rGO thin films.

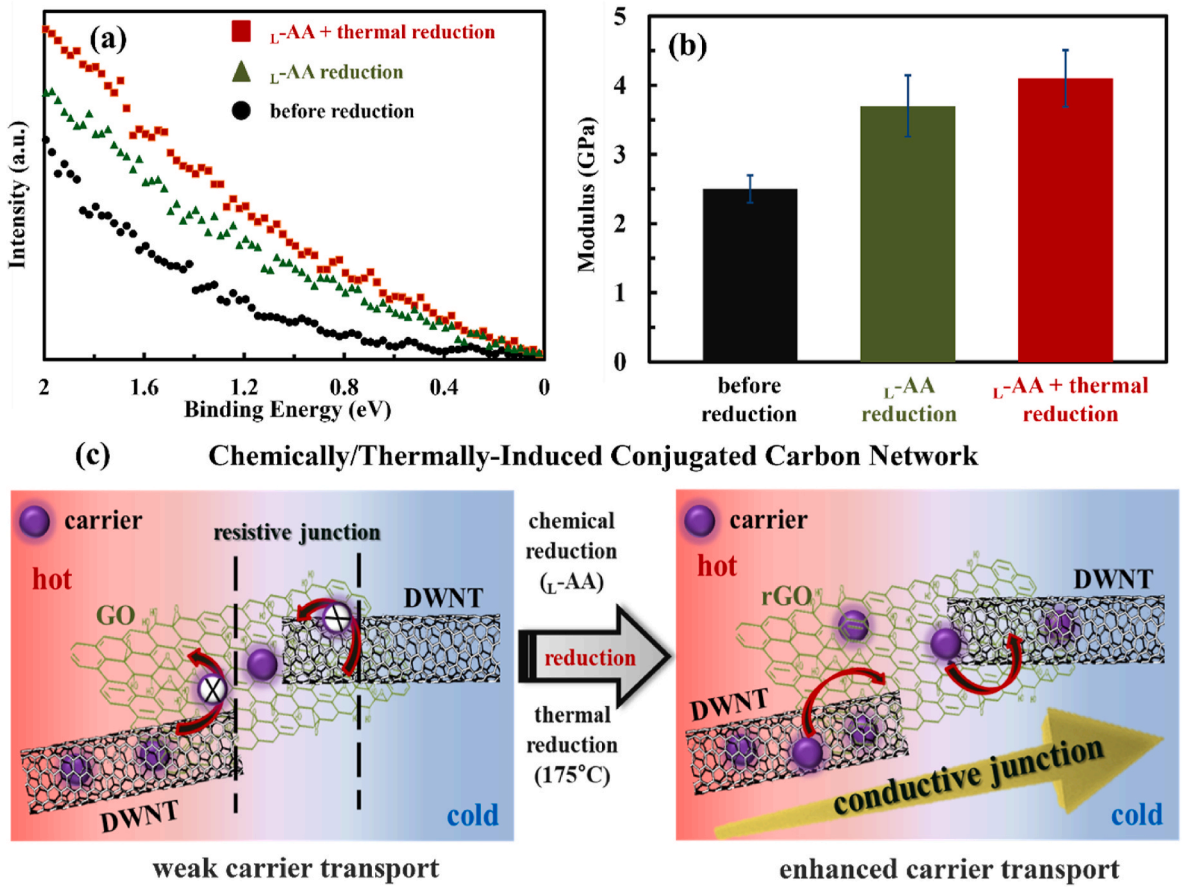

Fig. 8. (a) UPS spectra and (b) elastic modulus of spin-coated PVPS/DWNT-GO thin films before and after reduction treatments, and (c) schematic demonstration of carrier transport in the PVPS/DWNT-GO and PVPS/DWNT-rGO thin films.

(Table S3). Specifically, PVPS/DWNT-rGO films chemically reduced by $_L$-AA exhibited a 0.13 eV higher work function relative to untreated GO-based composites, suggesting an upward shift of the HOMO edge and indicating the E_f positioned lower relative to the vacuum level. Subsequent thermal reduction following the chemical reduction further increased the work function by an additional 0.12 eV, emphasizing a greater upward shift of the HOMO. These changes suggest that the combined chemical and thermal reduction processes effectively modified the electronic structure, enhancing p-type characteristics and thereby significantly contributing to the increased S in the multilayer PVPS/DWNT-rGO nanocomposites [47,48]. Nanoindentation results (Fig. 8(b)) revealed that the elastic modulus of chemically reduced PVPS/DWNT-rGO thin films was 3.72 GPa, which is more than 1.46 times higher than that of unreduced films (2.54 GPa). A subsequent thermal reduction following chemical reduction with $_L$-AA further enhanced the mechanical properties, yielding an elastic modulus of 4.17 GPa. The improvement in mechanical performance observed after combined chemical ($_L$-AA) and thermal reduction treatments is attributed to the formation of a densely packed nanostructure. To assess the mechanical robustness of the spin-coated multilayers, we performed

repeated bending (radius = 1.5 cm) and twisting tests on 8 BL PVPS/DWNT-rGO films deposited on flexible PET substrates. After 100 cycles of deformation, the electrical resistance increased by only ~10 %, demonstrating excellent mechanical flexibility and stable charge transport. As shown in Fig. S12, no visible cracks or delamination were observed during deformation. These results collectively support the mechanical reliability of the multilayer films for flexible TE applications. Carbon nanotubes enveloped by GO sheets are uniformly and directionally aligned throughout the multilayer films, significantly enhancing the mechanical behavior. Furthermore, the reduction of GO to rGO restores the intrinsic sp^2 carbon networks, improving mechanical stiffness through enhanced π–π interactions among graphene sheets. Additionally, improved load-transfer efficiency and stronger interfacial adhesion among the polymer matrix, DWNT, and rGO sheets are achieved. The reduction process substantially decreases oxygen-containing functional groups on GO, leading to more robust interfacial bonding and creating an effective load-bearing network that significantly contributes to the observed increase in elastic modulus.

Based on the above results, the proposed carrier transport mechanism is schematically illustrated in Fig. 8(c). The substantial enhancement observed in the TE performance of spin-coated LbL multilayer films can be fundamentally attributed to the strategic manipulation of their conjugated carbon architecture through controlled reduction treatments. Initially, the GO-based multilayers inherently possess numerous oxygen-containing functional groups, causing significant disruption to the conjugated sp^2 carbon domains. Chemical reduction via $_L$-AA effectively removes these oxygen functionalities, thereby restoring extensive π-conjugation networks and reducing energy potential barriers at the interfaces. This conversion from GO to rGO not only enhances the intrinsic electrical conductivity but also facilitates improved carrier transport due to minimized disorder and fewer structural defects within the conjugated carbon structures. Thermally assisted reduction treatments applied subsequent to chemical reduction significantly further extend the conjugation domains, thus strengthening the conductive network throughout the multilayers. The LbL assembly involving quasi-one-dimensional polymers, one-dimensional DWNT, and two-dimensional rGO sheets enables the formation of complex hierarchical interfaces within the composite. These abundant interfaces function as selective energy filters, preferentially scattering low-energy carriers while allowing high-energy carriers to pass unimpeded under temperature gradients, thereby enhancing the S [49,50]. Additionally, the energy-dependent carrier scattering across the well-defined multilayer interfaces provides efficient thermal-to-electrical energy conversion, exploiting the synergistic benefits of structural hierarchy and optimized electronic transport. Interestingly, the S of PVPS/DWNT-GO multilayers was found to increase after sequential chemical and thermal reduction, despite typical reductions in S observed in pristine GO. This behavior is attributed to the synergistic contributions of: (i) enhanced carrier mobility dominating over carrier concentration changes, (ii) improved π-conjugation and reduced structural disorder confirmed by Raman and XPS analyses, (iii) selective energy filtering at the hierarchical interfaces between DWNT, rGO, and PVPS, and (iv) modifications to the electronic density of states near the Fermi level, as indicated by UPS measurements. These factors collectively promote a favorable electronic transport environment that increases both σ and S simultaneously. GO typically exhibits low S values (5–10 μV/K), while rGO shows broader variation (10–60 μV/K) depending on reduction level and defect concentration as summarized in Table S4. DWNTs have been reported to possess moderate p-type thermopower (~30–40 μV/K). These values support our interpretation that the observed enhancement in S after reduction is a result of synergistic interfacial interactions, improved electronic structure, and increased carrier mobility within the multilayered PVPS/DWNT-rGO films. Consequently, the meticulous engineering of chemical and thermal reduction steps combined with the rational design of the multilayer architecture synergistically boosts the TE performance, highlighting the profound potential of these organic materials for advanced energy harvesting applications.

4. Conclusion

This work demonstrates a high-performance organic TE material using a spin-assisted LbL assembly approach to fabricate polymer nanocomposites. Spin-coated PVPS/DWNT-GO multilayers exhibited uniform growth and controlled thickness, forming interconnected, 3D carbon nanotube networks bridging GO platelets. These nanostructured networks facilitated improved electrical conduction pathways essential for efficient TE performance. Chemical reduction using $_L$-AA effectively removed oxygen functional groups from GO, significantly improving σ and S. Subsequent thermal treatment further boosted the σ by enhancing π-conjugation, substantially minimizing structural defects and disorder in the films, as evidenced by Raman spectroscopy and XPS analysis. Hall effect measurements confirmed that the remarkable increase in σ and S primarily originated from significantly enhanced carrier mobility due to the highly ordered, conjugated carbon structure. After chemical reduction with $_L$-AA and subsequent thermal treatment, an 8 BL PVPS/DWNT-rGO thin film achieved remarkable σ (556 S/cm) and S (105 μV/K), resulting in a high PF (612.5 $\mu W/m \cdot K^2$) at room temperature. This study underscores the potential of spin-assisted LbL assembly combined with eco-friendly reduction treatments to advance scalable and sustainable organic TE materials, offering promising applications in wearable devices and industrial waste-heat harvesting, contributing significantly toward environmentally friendly energy technologies.

CRediT authorship contribution statement

Sanghoon Jeong: Methodology, Investigation, Data curation, Conceptualization. **You-yeong Byun:** Investigation, Formal analysis, Conceptualization. **Junho Jang:** Resources, Formal analysis, Data curation, Conceptualization. **Mario Culebras:** Resources, Methodology, Investigation, Data curation, Conceptualization. **Jung Sang Cho:** Writing – original draft, Investigation, Data curation, Conceptualization. **Chungyeon Cho:** Writing – review & editing, Writing – original draft, Visualization, Project administration, Investigation, Data curation, Conceptualization.

Declaration of competing interest

The authors declare that they have no known competing financial interests or personal relationships that could have appeared to influence the work reported in this paper.

Acknowledgements

This research was supported by Wonkwang University in 2025.

Appendix A. Supplementary data

Supplementary data to this article can be found online at https://doi.org/10.1016/j.mtener.2025.101936.

Data availability

No data was used for the research described in the article.

References

[1] B. Russ, A. Glaudell, J.J. Urban, M.L. Chabinyc, R.A. Segalman, Organic thermoelectric materials for energy harvesting and temperature control, Nat. Rev. Mater. 1 (2016) 1–14.
[2] W. Hussain, S. Algarni, G. Rasool, H. Shahzad, M. Abbas, T. Alqahtani, et al., Advances in nanoparticle-enhanced thermoelectric materials from synthesis to energy harvesting: a review, ACS Omega 9 (2024) 11081–11109.

[3] P. MohanKumar, V.J. Babu, A. Subramanian, A. Bandla, N. Thakor, S. Ramakrishna, et al., Thermoelectric materials-strategies for improving device performance and its medical applications, Sciences 1 (2019) 37.
[4] L. Wang, Y. Liu, Z. Zhang, B. Wang, J. Qiu, D. Hui, et al., Polymer composites-based thermoelectric materials and devices, Compos. B Eng. 122 (2017) 145–155.
[5] P. Wu, Z. He, M. Yang, J. Xu, N. Li, Z. Wang, et al., A review on flexible thermoelectric technology: material, device, and applications, Int. J. Thermophys. 42 (2021) 111.
[6] D. Zhang, W.Y.S. Lim, S.S.F. Duran, X.J. Loh, A. Suwardi, Additive manufacturing of thermoelectrics: emerging trends and outlook, ACS Energy Lett. 7 (2022) 720–735.
[7] J.L. Blackburn, A.J. Ferguson, C. Cho, J.C. Grunlan, Carbon-nanotube-based thermoelectric materials and devices, Adv. Mater. 30 (2018) 1704386.
[8] H. Wang, C. Yu, Organic thermoelectrics: materials preparation, performance optimization, and device integration, Joule 3 (2019) 53–80.
[9] J. Liang, R. Cui, X. Zhang, K. Koumoto, C. Wan, Polymer/carbon composites with versatile interfacial interactions for high performance carbon-based thermoelectrics: principles and applications, Adv. Funct. Mater. 33 (2023) 2208813.
[10] J. Li, A.B. Huckleby, M. Zhang, Polymer-based thermoelectric materials: a review of power factor improving strategies, J Materiomics 8 (2022) 204–220.
[11] C. Cho, N. Bittner, W. Choi, J.H. Hsu, C. Yu, J.C. Grunlan, Thermally enhanced n-type thermoelectric behavior in completely organic graphene oxide-based thin films, Adv. Electron. Mater. 5 (2019) 1800465.
[12] J. Wei, Z. Jia, Y. Wang, Y. Jiang, Z. Miao, Y. Zhou, et al., Enhanced thermoelectric performance of low carbon cement-based composites by reduced graphene oxide, Energy Build. 250 (2021) 111279.
[13] W. Yu, L. Sisi, Y. Haiyan, L. Jie, Progress in the functional modification of graphene/graphene oxide, RSC Adv. 10 (2020) 15328–15345.
[14] M. Kurian, Recent progress in the chemical reduction of graphene oxide by green reductants–A Mini review, Carbon Trends 5 (2021) 100120.
[15] B. Fadeel, C. Bussy, S. Merino, E. Vázquez, E. Flahaut, F. Mouchet, et al., Safety assessment of graphene-based materials: focus on human health and the environment, ACS Nano 12 (2018) 10582–10620.
[16] T. Kuila, A.K. Mishra, P. Khanra, N.H. Kim, J.H. Lee, Recent advances in the efficient reduction of graphene oxide and its application as energy storage electrode materials, Nanoscale 5 (2013) 52–71.
[17] K.K.H. De Silva, H.-H. Huang, R. Joshi, M. Yoshimura, Restoration of the graphitic structure by defect repair during the thermal reduction of graphene oxide, Carbon 166 (2020) 74–90.
[18] J.J. Richardson, M. Björnmalm, F. Caruso, Technology-driven layer-by-layer assembly of nanofilms, Science 348 (2015) aaa2491.
[19] K. Ariga, Y. Lvov, G. Decher, There is still plenty of room for layer-by-layer assembly for constructing nanoarchitectonics-based materials and devices, Phys. Chem. Chem. Phys. 24 (2022) 4097–4115.
[20] K. Ariga, J. Song, K. Kawakami, Layer-by-layer designer nanoarchitectonics for physical and chemical communications in functional materials, Chem. Commun. 60 (2024) 2152–2167.
[21] A.M. Ganjeh, J.A. Saraiva, C.A. Pinto, S. Casal, I. Gonçalves, Recent advances in nano-reinforced food packaging based on biodegradable polymers using layer-by-layer assembly: a review, Carbohydr. Polym. Tech. 7 (2024) 100395.
[22] K. Ariga, E. Ahn, M. Park, B.S. Kim, Layer-by-layer assembly: recent progress from layered assemblies to layered nanoarchitectonics, Chem. Asian J. 14 (2019) 2553–2566.
[23] A.C. Almeida, A.C. Vale, R.A. Pires, R.L. Reis, N.M. Alves, Layer-by-layer films based on catechol-modified polysaccharides produced by dip-and spin-coating onto different substrates, J. Biomed. Mater. Res. B 108 (2020) 1412–1427.
[24] M. Culebras, Y-y Byun, J. Jang, T.K. Lee, D. Choi, A. Serafin, et al., Enhanced thermoelectric performance in polypyrrole-based multilayer nanoarchitectures via thermal reduction, ACS Appl. Energy Mater. 7 (2024) 2351–2361.
[25] Y. Gao, H.W. Jing, S.J. Chen, M.R. Du, W.Q. Chen, W.H. Duan, Influence of ultrasonication on the dispersion and enhancing effect of graphene oxide–carbon nanotube hybrid nanoreinforcement in cementitious composite, Compos. B Eng. 164 (2019) 45–53.
[26] J. Kim, S.W. Kim, H. Yun, B.J. Kim, Impact of size control of graphene oxide nanosheets for enhancing electrical and mechanical properties of carbon nanotube–polymer composites, RSC Adv. 7 (2017) 30221–30228.
[27] C. Zhang, L. Ren, X. Wang, T. Liu, Graphene oxide-assisted dispersion of pristine multiwalled carbon nanotubes in aqueous media. TJ, Phys. Chem. C 114 (2010) 11435–11440.
[28] C. Cho, S. Qin, K. Choi, J.C. Grunlan, Improved thermoelectric power factor in completely organic nanocomposite enabled by L-ascorbic acid, ACS Appl. Polym. Mater. 1 (2019) 1942–1947.
[29] Y. Du, J. Yang, B.S. Thomas, L. Li, H. Li, S. Nazar, Hybrid graphene oxide/carbon nanotubes reinforced cement paste: an investigation on hybrid ratio, Constr. Build. Mater. 261 (2020) 119815.
[30] I. Lee, S. Kim, J.O. Shim, J.S. Cho, C. Cho, High flame retardancy of carbon nanotubes reinforced polyelectrolyte multilayered nanocomposites, J. Appl. Polym. Sci. (2025) e56967.
[31] M.N. Hyder, S.W. Lee, F.Ç. Cebeci, D.J. Schmidt, Y. Shao-Horn, P.T. Hammond, Layer-by-layer assembled polyaniline nanofiber/multiwall carbon nanotube thin film electrodes for high-power and high-energy storage applications, ACS Nano 5 (2011) 8552–8561.
[32] J.P.C. Trigueiro, G.G. Silva, F.V. Pereira, R.L. Lavall, Layer-by-layer assembled films of multi-walled carbon nanotubes with chitosan and cellulose nanocrystals, J. Colloid Interface Sci. 432 (2014) 214–220.
[33] B. Stevens, E. Dessiatova, D.A. Hagen, A.D. Todd, C.W. Bielawski, J.C. Grunlan, Low-temperature thermal reduction of graphene oxide nanobrick walls: unique combination of high gas barrier and low resistivity in fully organic polyelectrolyte multilayer thin films, ACS Appl. Mater. Interfaces 6 (2014) 9942–9945.
[34] Y-y Byun, J. Jang, M. Culebras, B.-S. Bae, J.S. Cho, Y.T. Park, et al., Conformation-dependent thermoelectric power factor of multilayer nanocomposites, Appl. Surf. Sci. 594 (2022) 153483.
[35] T. Nakashima, J. Zhu, M. Qin, S. Ho, N.A. Kotov, Polyelectrolyte and carbon nanotube multilayers made from ionic liquid solutions, Nanoscale 2 (2010) 2084–2090.
[36] M. Lindorf, K. Mazzio, J. Pflaum, K. Nielsch, W. Brütting, M. Albrecht, Organic-based thermoelectrics, J. Mater. Chem. A. 8 (2020) 7495–7507.
[37] Y. Zhang, W. Wang, F. Zhang, K. Dai, C. Li, Y. Fan, et al., Soft organic thermoelectric materials: principles, current state of the art and applications, Small 18 (2022) 2104922.
[38] M.T.Z. Myint, M. Hada, H. Inoue, T. Marui, T. Nishikawa, Y. Nishina, et al., Simultaneous improvement in electrical conductivity and Seebeck coefficient of PEDOT: PSS by N 2 pressure-induced nitric acid treatment, RSC Adv. 8 (2018) 36563–36570.
[39] Q. Jiang, C. Liu, D. Zhu, H. Song, J. Xu, H. Shi, et al., Simultaneous enhancement of the electrical conductivity and seebeck coefficient of PEDOT-block-PEG/SWCNTs nanocomposites, J. Electron. Mater. 44 (2015) 1585–1591.
[40] A.C. Faucett, J.M. Mativetsky, Nanoscale reduction of graphene oxide under ambient conditions, Carbon 95 (2015) 1069–1075.
[41] T.C. Chiang, F. Seitz, Photoemission spectroscopy in solids, Ann. Phys. 513 (2001) 61–74.
[42] A. Saha, S. Basiruddin, S.C. Ray, S. Roy, N.R. Jana, Functionalized graphene and graphene oxide solution via polyacrylate coating, Nanoscale 2 (2010) 2777–2782.
[43] M. Sun, G. Wang, X. Li, C. Li, Irradiation preparation of reduced graphene oxide/carbon nanotube composites for high-performance supercapacitors, J. Power Sources 245 (2014) 436–444.
[44] L. Al-Mashat, K. Shin, K. Kalantar-Zadeh, J.D. Plessis, S.H. Han, R.W. Kojima, et al., Graphene/polyaniline nanocomposite for hydrogen sensing, J. Phys. Chem. C 114 (2010) 16168–16173.
[45] A.C. Ferrari, J. Robertson, Interpretation of Raman spectra of disordered and amorphous carbon, Phys. Rev. B 61 (2000) 14095.
[46] I. Petsagkourakis, E. Pavlopoulou, E. Cloutet, Y.F. Chen, X. Liu, M. Fahlman, et al., Correlating the Seebeck coefficient of thermoelectric polymer thin films to their charge transport mechanism, Org. Electron. 52 (2018) 335–341.
[47] D.L. Stevens, A. Parra, J.C. Grunlan, Thermoelectric performance improvement of polymer nanocomposites by selective thermal degradation, ACS Appl. Energy Mater. 2 (2019) 5975–5982.
[48] S.L. Kim, K. Choi, A. Tazebay, C. Yu, Flexible power fabrics made of carbon nanotubes for harvesting thermoelectricity, ACS Nano 8 (2014) 2377–2386.
[49] N. Nandihalli, C.-J. Liu, T. Mori, Polymer based thermoelectric nanocomposite materials and devices: fabrication and characteristics, Nano Energy 78 (2020) 105186.
[50] J.-A. Yao, X.-X. Peng, Z.-K. Liu, Y.-F. Zhang, P. Fu, H. Li, et al., Enhanced thermoelectric properties of bilayer-like structural graphene quantum dots/single-walled carbon nanotubes hybrids, ACS Appl. Mater. Interfaces 12 (2020) 39145–39153.